Array Sensing Using Electromagnetic Method for Detection of Smelting in Submerged Arc Furnaces

WeiLing Liu[1], XiaoHong Han[2], LingZhen Yang[3], and XiaoMing Chang[1]*

[1]College of Computer Science and Technology, Taiyuan University of Technology, No. 79 Yingze West Street, Taiyuan 030024, Shanxi, PR China
[2]College of Mechanical Engineering, Taiyuan University of Technology, No. 79 Yingze West Street, Taiyuan 030024, Shanxi, PR China
[3]College of Physics and optoelectronics, Taiyuan University of Technology, No. 79 Yingze West Street, Taiyuan 030024, Shanxi, PR China

In this paper, we propose an array sensing detection method for smelting of submerged arc furnaces (SAF) based on electromagnetic radiation. AC magnetic field generated by electrode currents and molten currents in the furnace is reflected outside of the furnace. According to the spatial distribution of electromagnetic field a radiation model of SAF is built. We design a 3D magnetic field sensing array system in order to collect the magnetic field information. Through the collected information, the current distribution characteristics of SAF are described and the key parameters of smelting are obtained. Theoretical simulation and field test show that the curves acquired by the sensing array can accurately reflect the information of the relative displacement when the relative displacement between the array and electrode is 10 cm. Compared with the detection method of 3D single point, the proposed array sensing method of magnetic field obtains better results in terms of real-time and accuracy, and has good practical value for industrial measurement.

Keywords : submerged arc furnace, key parameters of smelting, magnetic field, array sensing

1. Introduction

Submerged arc furnace (SAF) is an industrial electric furnace which gets power through graphite electrodes. The electric arcs emerge between the furnace burden and the electrode tip, which makes the electrical energy change into heat energy. The obtained heat energy can be used to melt ores. By smelting the ores many types of ferroalloys can be obtained such as ferrosilicon, ferromanganese, ferrochrome, ferrotungsten, and silicon-manganese alloys, and so on [1-3]. However, a typical SAF consumes a great deal of electrical energy (approximately 450 kWh/ ton) in the process of smelting. Therefore, it is necessary to study the SAF smelting processes from the economic and environmental points of view [4-6].

Smelting in SAF is an extremely complicated process involving physical-chemical reactions and heat exchanges [7-9]. The fluctuation of the furnace condition occurs frequently under the influence of many factors. Thus measurement technique and detection system for the furnace are necessary for operators to analyze the furnace condition accurately and take measures opportunely to guarantee the stable running of the furnace [10, 11]. In practice, the furnace condition is observed through simple instruments, personal experiences or naked eyes, which are difficult to get the optimal smelting parameters and thus lower production efficiency [12]. To overcome the drawbacks, lots of methods have been put forward to measure these key parameters. However some of these methods get the measurement through indirect calculation and speculation [13-16]. Other methods only get the position of electrode tip roughly [17, 18].

We propose a non-contact array sensing detection method of magnetic field. Based on the inner structure of SAF and electromagnetism, a magnetic field radiation model of SAF is established. We analyze the problems existing in the 3D single point detection method of magnetic field and then propose a model of array detection. The spatial distance of the detection points is calculated and determined through probing the distributing rule of

magnetic field in SAF. The theoretical analysis and preliminary experiments show that the proposed method gets better results in real-time and precision compared with the single point 3D detection method. Using our proposed method, the maintenance of the equipment is more convenient in later periods than the single point 3D detection method.

The rest of paper is organized as follows. Section 2 describes the measuring principle and system structure. In Section 3, determination of the spatial distance of detection points is introduced. Thereafter experimental results are presented in Section 4, and conclusions are given in Section 5.

2. Measuring Principle and System Structure

2.1. Magnetic field radiation model

The hearth structure of SAF is shown in Fig. 1 [19-21].

The electric arc is generated between electrode tip and molten bath shown in Fig. 1. The molten alloys gather in molten bath, and the top of molten bath surface, is the position of liquid level.

Through the electrodes, large currents flow into the furnace, in which the circuit can be regarded as two types of loop: star circuit loop and triangle circuit loop [22, 23], and the two types of loop can be equivalently transformed. In this paper we take the triangle loop as an example to analyze the circuit model. Based on electromagnetic
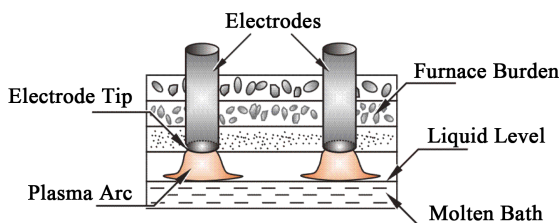

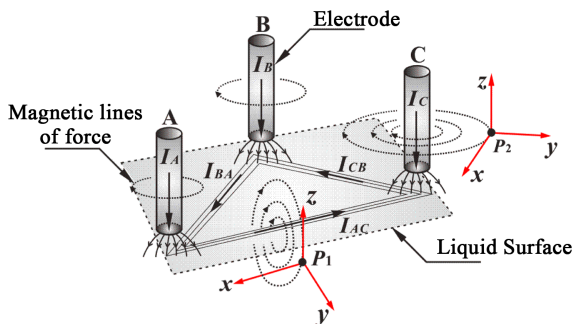**Fig. 1.** (Color online) The hearth structure of SAF.

Fig. 2. (Color online) The magnetic field radiation model of SAF.
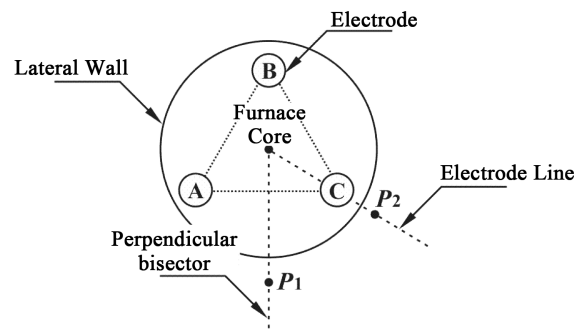

Fig. 3. The plan view of the SAF.

principles, magnetic field radiation model of SAF can be built, as shown in Fig. 2.

In Fig. 2, the electrode currents I_A, I_B, I_C flow into the furnace along each electrode and near the liquid surface they form a triangle circuit loop composed of the currents I_{AC}, I_{CB}, I_{BA}. The two points P_1 and P_2 are the measured origins, respectively. I_{AC} is the molten bath current parallel to the x-axis component B_x at point P_1. I_C is the electrode current parallel to the z-axis component B_z at point P_2. In order to describe conveniently, the concepts of electrode line and perpendicular bisector are defined as shown in Fig. 3.

In Fig. 3 the plan view of SAF is given. On the plane parallel to the molten bath surface, a regular triangle is generated through connecting three vertices of electrodes, and the core of SAF is the center of the triangle. The line connecting the electrode and the furnace core is called electrode line. The vertical of each edge of the regular triangle is termed as perpendicular bisector. It can be seen that the perpendicular bisector is parallel to y-axis component B_y of point P_1, and the electrode line is parallel to y-axis component B_y of point P_2.

2.2. 3D single point detection model

The 3D single point detection system of magnetic field shown in Fig. 4 is composed of 3D probe, main control unit (MCU), and PC.

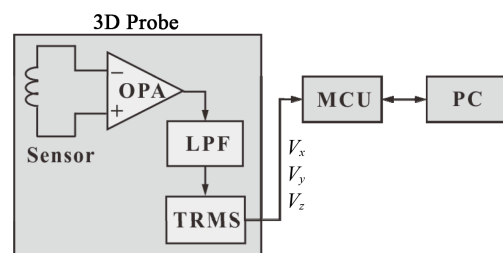In Fig. 4, the upper PC gives the control commands, and MCU collects and processes the 3D probe magnetic

Fig. 4. The architecture of 3D single point detection system.

field information and sends the information back to the PC. 3D probe is composed of the magnetic sensor, operational amplifier (OPA), low-pass filter (LPF), and true RMS conversion circuit (TRMS).

For any system in which high real-time is demanded, the delay time caused by information transmission is unavoidable and cannot be ignored [24]. For the 3D single point detection system, sampling and processing time T_{SP} is analyzed and expressed as Eq. (1).

$$T_{SP} = \sum_{i=1}^{5} T_{Si} \tag{1}$$

In Eq. (1), T_{S1}, T_{S2}, T_{S3}, T_{S4}, T_{S5} are the time of sensor collection, signal amplification, low-pass filtering, TRMS conversion and MCU processing, respectively. In the practical engineering problems, T_{S1}, T_{S2}, T_{S3} and T_{S5} are all in milliseconds level. However, TRMS conversion circuit adopts the principle of integral, and the higher the output accuracy is required, the longer the processing time that TRMS conversion takes will be. Generally, the time, which it takes for the TRMS conversion circuit to convert once until to stable states, T_{S4}, is approximately equal to $T_{S4} \approx 3{\sim}5$ s. If only taking the inflence of the TRMS conversion time T_{S4} into account, the single sampling and processing time T_{SP} is approximately equal to $T_{SP} \approx T_{S4} \approx 3{\sim}5$ s.

In the 3D single point detection way of magnetic field, to attain the key parameters in the furnace, the data of several detection points needs to be acquired. Namely when the sampling work of every point is finished, the 3D probe needs to be moved to next detection point. To sample N points using the 3D single point detection system, the time T_{NS} is presented as Eq. (2).

$$T_{NS} = N \times T_{SP} + (N-1) \times T_{MOV} \tag{2}$$

where N is the number of sampling points. T_{MOV} is the moving time between adjoining sampling points of the 3D single point detection system. For the practical engineering problems, $T_{MOV} \geq 3$ s.

In conclusion, the minimum values of the sampling and processing time T_{SP} and the moving time T_{MOV} are approximately equal to $T_{SP\,(min)} \approx 3$ s and $T_{MOV\,(min)} \approx 3$ s, respectively. We apply the parameters mentioned above to Eq. (2) to get the minimum value of the time T_{NS} which is given as Eq. (3).

$$T_{NS(min)} \approx 6N - 3 \tag{3}$$

From Eq. (3), the collecting time T_{NS} increases with the number of sampling points. When the total measurement length is 150 cm and sampling spatial distance is 10 cm, the number of sampling points is 15. According to Eq.

(3), the collecting time T_{NS} is at least 87s. However, during the period of 87s, the furnace condition may have changed greatly, so this detection way can't truly reflect the furnace condition. Moreover, there still exist many kinds of errors in the 3D single point detection method, and the factors which produce errors mainly include the following aspects:

(1) Due to the trembling of the mechanical equipments, it is difficult to keep measuring baseline and datum plane united in the process of moving.

(2) For moving mechanical equipments, it is difficult to keep uniformity of detection points for a long time.

(3) Moving mechanically will increase the failure rate of testing parts of the system.

(4) Considering the measuring accuracy and the maintenance of equipment in later periods, more complexity in mechanical construction design is required.

Due to the above limitations, the 3D single point detection system of magnetic field is difficult to satisfy the measurement demand in the real industrial field.
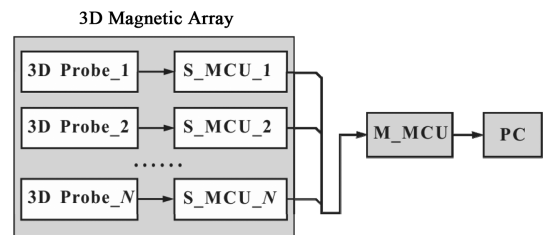
2.3. Modelling the array sensing detection

To improve the performance in terms of real-time and precision, combining with the principle of datum plane unity in the theory of instrument precision [25], we propose an array sensing detection method of magnetic field, and the system constitution is shown in Fig. 5.

In Fig. 5, 3D magnetic array is composed of N 3D probes arranged in a linear and uniform way and every probe is equipped with a sub-microcontroller (S_MCU). When main-microcontroller (M_MCU) receives the commands from PC and triggers N S_MCUs simultaneously, the N S_MCUs will collect the three-dimensional magnetic field data using the 3D probes and send the information back to PC.

From Fig. 5, there is no moving time in the array sensing detection way. When N S_MCUs gather the data simultaneously, the delay time T_{NA} is equal to the sampling and processing time of 3D single point detection system T_{SP}, as shown in Eq. (4).

$$T_{NA} \approx T_{SP} \tag{4}$$

Fig. 5. The constitution of the array sensing detection system of magnetic field.

From Eq. (4), the acquisition time of array sensing detection system is equal to $T_{NA} \approx 3\sim5$ s, and is independent of the number of sampling points. Therefore, the real-time performance of array sensing detection is far better than single point detection. Moreover, there does not exist the moving problem of mechanical equipment in the array detection way, which guarantees the homogeneity of the sampling interval and the unity of measuring baseline and datum plane. Our proposed method simplifies the design of mechanical connection structure and makes the maintenance of the equipment easy in later periods. So the testing precision and collection efficiency is greatly improved.

3. Design of Array Sensor Structure

3.1. Modelling the magnetic field distribution

The detected point P_1 in Fig. 2 is assumed to be the origin o, and several detection points (S_1, S_2, …, S_m, …, S_i) are chosen from the z-axis. In these detection points, the point S_m, which overlaps with the point P_1, locates on the geometric plane generated by current I_{AC}, I_{CB}, and I_{BA}. The magnetic induction intensity distribution at point P_1 in perpendicular bisector is shown in Fig. 6 under the influence of the magnetic field produced by current I_{AC}.

From Fig. 6 the relation between the distance r from the detection point S_i to the current I_{AC} and the height of point S_i is presented in Eq. (5):

$$r^2 = h^2 + a^2 \qquad (5)$$

Where h_i is the height of detection point S_i; a is the distance from the origin o to the pathway of current I_{AC}. Because the detection point S_i is at the perpendicular bisector, the distance from point S_i to the starting point of current I_{AC} equals the distance from point S_i to the end point which is given by Eq. (6).

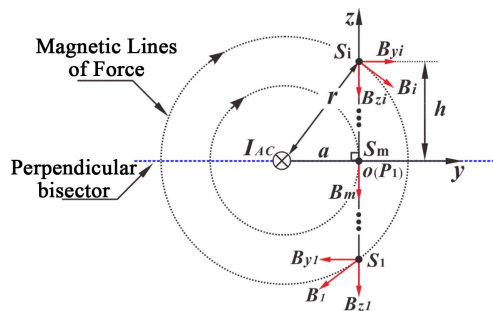$$R = \sqrt{\left(\frac{L_{AC}}{2}\right)^2 + r^2} \qquad (6)$$

Fig. 6. (Color online) The diagram of magnetic induction intensity distribution of the current I_{AC}.
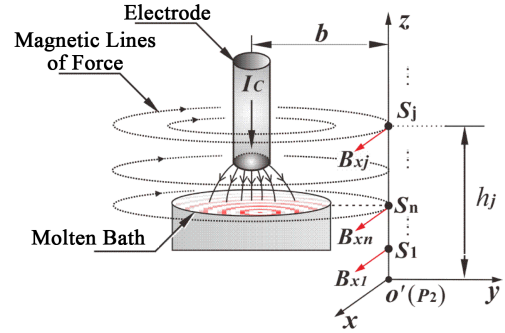

Fig. 7. (Color online) The diagram of magnetic induction intensity distribution at detected point P_2.

Where L_{AC} is the length of the straight wire carrying current I_{AC}.

From Fig. 6, it can be seen that the magnetic flux density components of the detection point S_i along the x, y and z-axis are B_{xj}, B_{yi}, and B_{zi} which are given as Eq. (7).

$$\begin{cases} B_y = \dfrac{\mu_0 I_{AC} L_{AC} h}{4\pi R r^2} \\[2mm] B_x = 0 \\[2mm] B_z = \dfrac{\mu_0 I_{AC} L_{AC} a}{4\pi R r^2} \end{cases} \qquad (7)$$

The detected point P_2 in Fig. 2 is assumed to be the origin o', and several detection points (S_1, …, S_n, …, S_j…) are chosen on the z-axis. h_j is the height of the point S_j, and h_n is the height of the molten bath surface. The magnetic induction intensity distribution at point P_2 on electrode line is shown in Fig. 7 under the influence of the magnetic field produced by the current I_C.

From Fig. 7, the magnetic flux density components of the detection point S_j along the x, y and z-axis are B_{xj}, B_{yj}, and B_{zj} which are presented as Eq. (8):

$$\begin{cases} B_{xj} = 0 & (1 \le j < n) \\[2mm] B_{xj} = \dfrac{\mu_0}{4\pi} \displaystyle\int_{(L_C)} \dfrac{I_C d\vec{l} \times \vec{r}}{b^2} & (j \ge n) \\[2mm] B_{yj} = B_{zj} = 0 \end{cases} \qquad (8)$$

in which b is the distance from detection points to the pathway of current I_C. L_C is the length of current I_C.

The currents turn to transverse direction below the liquid surface [5, 2, 9], so $B_{xj} = 0$ ($1 \le j < n$), and over the liquid surface $B_{xj} \ne 0$ ($j \ge n$). In this case both B_{yj} and B_{zj} are the constant 0. Thus, the key parameters, including liquid level and electrode tip, can also be obtained at the point P_2.

3.2. Calculating the spatial sampling interval of detection points

According to the theory of digital imaging detection technology [26], low density of sampling interval causes the artifact. And the denser sampling interval can achieve the higher spatial resolution and more authentic furnace condition. However, an excess of redundancy leads to a waste of resources. We take the z-axis component B_z as an example to discuss how to determine the spatial sampling interval. h_i and h_{i+1} is the height of the detection point S_i and S_{i+1} respectively. B_{zi} and $B_{z(i+1)}$ is the z-axis component of magnetic flux density at the detection point S_i and S_{i+1} respectively. In this system, with $\Delta h = h_{(i+1)} - h_i$ being the spatial interval, the variation of B_z between adjacent points is defined as $\Delta B = B_{z(i+1)} - B_{zi}$. The distribution characteristic of B_z and the relation between ΔB and Δh is given in Fig. 8.

In Fig. 8, the tangent line at detection point S_i is S_iT. Based on the basic method of local linearization of the nonlinear function in differential calculus [27], in the vicinity of the detection point S_i, the tangent segment S_iP can be an approximate substitute for the curved section S_iS_{i+1}, namely dB is approximated as ΔB. Thus, when the derivative of some point $B_z'(h) \neq 0$, the relation between dB and Δh can be expressed by Eq. (9), where the adjoining points interval $\Delta h << a$.

$$\left| \Delta B \right| \approx dB = \left| B_z'(h) \right| \Delta h \tag{9}$$

δ is assumed to be the resolution of the magnetic array sensors, and once the hardware development is finished, δ is a constant. While the variation of $B_z \left| \Delta B \right| < \delta$, it is beyond the recognition capability of the hardware equipment. Therefore, it is reasonable to take $\left| \Delta B \right| = \delta$. So Δh can be obtained with Eq. (10) dealing with engineering:

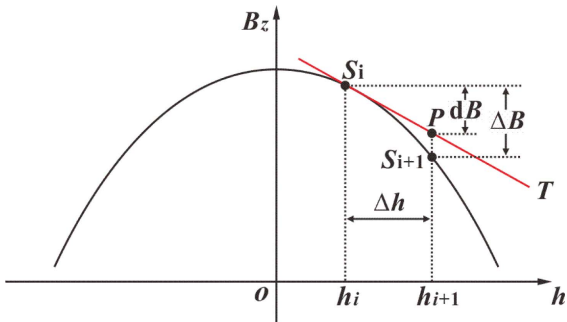$$\Delta h \approx \frac{\delta}{\left| B_z'(h) \right|} \tag{10}$$

Fig. 8. (Color online) The distribution characteristic of B_z and the relation between ΔB and Δh.

From Eq. (10), among the detection points (S_1, S_2, …, S_m, …, S_i, …), the point at which the maximum value of change rate of magnetic induction $\left| B_z'(h) \right|_{max}$ locates has strict requirement that spatial sampling interval, Δh, is equal to the minimal value. In practical application, d is defined as spatial sampling distance which is determined by Eq. (11):

$$d \leq \Delta h_{min} \approx \frac{\delta}{\left| B_z'(h) \right|_{max}} \tag{11}$$

With B_{xj}, B_{yi}, and B_{zi} of the point S_i given by Eq. (7), it is relatively simple to obtain the change rate of the magnetic flux density using differential calculus with Eq. (12):

$$\begin{cases} (B_y)' = \dfrac{\mu_0 I_{AC} L_{AC}}{2\pi R r^2} \left(\dfrac{1}{2} - \dfrac{h^2}{r^2} - \dfrac{h^2}{2R^2} \right) \\ (B_x)' = 0 \\ (B_z)' = \dfrac{\mu_0 I_{AC} L_{AC} ah}{2\pi R r^2} \left(\dfrac{1}{2R^2} - \dfrac{1}{r^2} \right) \end{cases} \tag{12}$$

Since the detection points are outside of the furnace, μ_0 is equal to $4\pi \times 10^{-7}$ H/m, and I_{AC} is approximately equal to 40 kA [5]. According to the environmental observation in real scene, the values of the parameter a and L are set to $a \approx 8.5$ m and $L_{AC} \approx 1.6$ m, respectively. We apply the parameters mentioned above to Eq. (12) and calculate the maximal change rate of the magnetic flux density, as Eq. (13) shows below:

$$\begin{cases} \left| B_y'(h) \right|_{max} = 1.04 \text{ mGs/cm} \\ \left| B_z'(h) \right|_{max} = 0.89 \text{ mGs/cm} \end{cases} \tag{13}$$

In this paper the resolution of the magnetic array sensors δ equals 12 mGs. we apply the parameters in Eq. (13) to Eq. (10) and Eq. (11), and then the minimum of Δh in y-axis ans z-axis is computed as follows:

$$\begin{cases} \Delta h_{y\,min} \approx 11.5 \text{ cm} \\ \Delta h_{z\,min} \approx 13.5 \text{ cm} \end{cases} \tag{14}$$

From Eq. (14), when $d \leq 11.5$ cm, we can get the required signal. Considering the restrictions in terms of hardware design, the spatial sampling distance d is set to 10 cm.

3.3. The real product structure of magnetic field arrays
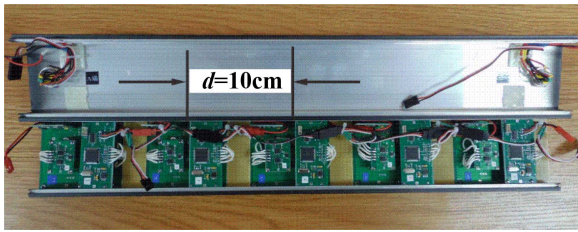
The magnetic field array with the sensors in series is

Fig. 9. (Color online) The internal structure of the magnetic array unit.

Fig. 10. (Color online) The real product of magnetic field arrays.

Fig. 11. (Color online) The measuring schematic diagram in real industrial field.

Fig. 12. (Color online) The experimental scene in industrial field.

composed of some array units, one of which consists of five 3D probes. The internal structure of the magnetic array unit is shown in Fig. 9.

In one array unit, the spatial interval between adjacent 3D probes is 10 cm. Fig. 10 shows the real product photo of magnetic field arrays.

In Fig. 10, the length of every array is 180 cm in which the length of power supply and MCU is 30 cm.

3.4. Experiments in real industrial field

We perform real measurements on the SAF of ferrosilicon manganese alloy (6300 KVA) at a metallurgical company of Yinchuan city in China. According to the theoretical analysis, the distribution of B_y and B_z in perpendicular bisector contains the information of liquid level, and the distribution of B_x on electrode line also contains the key information of liquid level. Through multiple experiments, we choose the test site between perpendicular bisector and electrode line, and the angle is set to about 20° between the electrode line and the line connecting the test site and the furnace core. The magnetic array which is about 6 m away from the lateral wall is vertically placed. The measuring schematic diagram in real industrial field is shown in Fig. 11.

In Fig. 11, we set the origin o beneath the array sensor S_1 10 cm, and the measuring range covers the electrode tip. The experimental scene in industrial field is shown in Fig. 12.
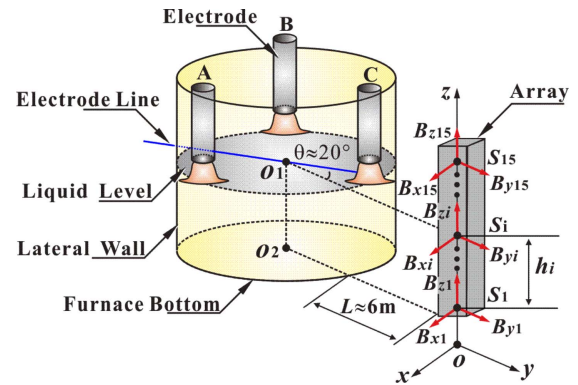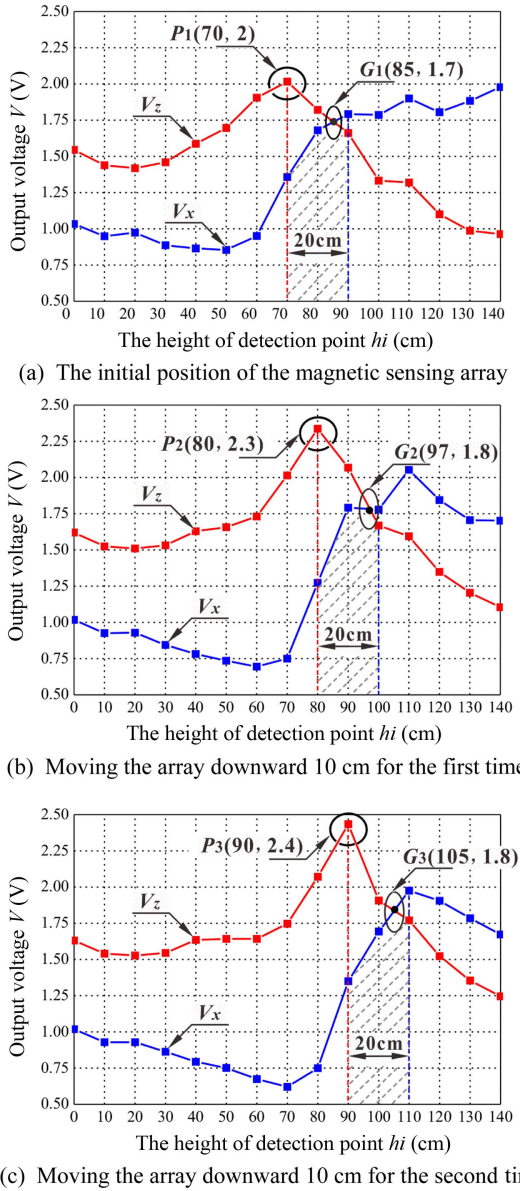
It should be noted that the relationship between the output voltage and the magnetic flux intensity has not been calibrated due to the limit of testing equipment. So we only present measuring results through the output voltage of V_x, V_y, and V_z.

4. Results and Discussion

In the testing experiments, the magnetic flux density components V_y of electrode currents and molten currents are obtained at the same time at the detection point. Due to the mixture of the two components, it is difficult to analyze them. Therefore, we only analyze the $h{\sim}V_x$ curve and $h{\sim}V_z$ curve. Moreover, the relative displacement is changed by moving the magnetic sensing array or by lifting and lowering electrodes. The testing results show that the curves of $h{\sim}V_x$ and $h{\sim}V_z$ move towards right while moving the magnetic sensing array downward, and it is shown in Fig. 13.

In Fig. 13, P_N is at the peak point of the $h{\sim}V_z$ curve and G_N locates the cross point of the curves of $h{\sim}V_x$ and $h{\sim}V_z$

(a) The initial position of the magnetic sensing array

(b) Moving the array downward 10 cm for the first time

(c) Moving the array downward 10 cm for the second time

Fig. 13. (Color online) The analysis on testing results.

for $N = 1, 2, 3$. There is a shadow region with the width 20 cm in Fig. 13. The left side of the shadow region corresponds to the peak point P_N, and the right side locates near the right of the cross point G_N. From Fig. 13 it can be found that:

(1) The $h\sim V_z$ curve looking like a shape of bell has close correlation to Eq. (7). It can be inferred that the abscissa value of the peak point P_N can be regarded as the height of the transverse current I_{AC} that lies beneath the molten bath surface.

(2) The $h\sim V_x$ curve shows an monotonous increasing trend in the range of 20 cm from the beginning with left side of the peak point P_N which is about 10 cm away from P_N. It reflects the position of the electrode tip and

the changes of the current intensity from the liquid level to the electrode tip.

(3) The abscissa value of the cross point G_N indicates that the position of G_N is near the electrode tip. And at the right of the point G_N the $h\sim V_x$ curve tends to stable. Based on the above analysis, we can conclude that the right region of the point G_N lies above the electrode tip.

(4) In Fig. 13, the difference values of the abscissa at the peak point P_N and the cross point G_N are both 10 cm. It can be seen that when the relative displacement between the magnetic sensing array and the electrode is 10 cm, the relative displacement of the $h\sim V_x$ curve and $h\sim V_z$ curve is also 10 cm.

5. Conclusions

This paper proposes an array sensing detection method for smelting parameters of SAF based on electromagnetism. Compared with single point 3D detection of magnetic field, the proposed approach has the higher efficiency and the superiority over real-time performance and precision. Theoretical analysis show that if the spatial sampling distance of the magnetic sensing array is set to 10 cm, the distribution characteristics of SAF can be reflected, and some key parameters in the smelting process can be achieved. Moreover, experimental results show that the relative displacement can be measured precisely by the collected information through the magnetic array when the relative displacement between the array and the electrode is 10 cm.

References

[1] C. X. Li, F. Wang, and J. C. San, Cast Alloy and Melting, Chemical Industry, Beijing (2012) pp. 126-129.
[2] F. Martell, M. Ramirez, A. Llamas, and O. Micheloud, ISIJ International. **53**, 743 (2013).
[3] M. Kadkhodabeigi, H. Tveit, and J. S. Tore, ISIJ International. **51**, 193 (2011).
[4] F. Martell, A. Deschamps, R. Mendoza, M. Melendez, A. Llamas, and O. Micheloud, ISIJ International. **51**, 1846 (2011).
[5] M. Ramirez, J. Alexis, G. Trapaga, and P. Jonsson, ISIJ International **41**, 1146 (2001).
[6] V. Logar and I. Skrjanc, ISIJ International **52**, 1924 (2012).

[7] A. C. Mulholland, P. J. Breretonstiles, and C. J. Hockaday, J. S. Afr. I. Min. Metall. **109**, 601 (2009).

[8] N. N. Zhang, Z. J. Wang, and D. J. Zhang, IEEE. Comput. Mechatr. Contr. Electr. Eng. **3**, 108 (2010).

[9] J. Alexis, M. Ramirez, G. Trapaga, and P. Jonsson, ISIJ. International **40**, 1089 (2000).

[10] S. Dwarapudi, V. Tathavadkar, B. C. Rao, T. K. S. Kumar, T. K. Ghosh, and M. Denys, ISIJ International **53**, 9 (2013).

[11] T. Ito, J. Yotsuji, and A. Nagamune, ISIJ International **54**, 2618 (2014).

[12] Y. L. Wang, Metallurgy of Iron and Steel [M]. Metallurgical Industry, Beijing (2013) pp. 267-269.

[13] J. Zhang, S. J. Chu, and Z. S. Li, Ferro-Alloys **3**, 5 (2014).

[14] S. M. Kang, Ferro-Alloys **2**, 30 (2012).

[15] J. M. Wu, Q. X. Wang, Z. Q. Xu, and Q. H. Zhu, Contr. Instru. Chem. Indus. **41**, 181 (2013).

[16] Y. Wang, Z. Z. Mao, H. X. Tian, Y. Li, and P. Yuan, J. Cent. South. Univ. T. **17**, 560 (2010).

[17] Y. Bai, Q. Wang, F. R. Meng, and H. Y. Wang, J. ChangChun. University. T **33**, 383 (2012).

[18] Z. H. An, Ms. D. Thesis, Changchun University of Technology, China (2010).

[19] S. J. Chu, S. L. Zeng, and Z. C. Huang, Ferro-Alloys **2**, 13 (2009).

[20] S. J. Chu, X. E. Bao, and Z. S. Li, Ferro-Alloys **3**, 22 (2013).

[21] A. S. Hauksdottir, T. Soderstrom, Y. P. Thorfinns son, and A. Gestsson, IEEE.T. Contr. Syst. T. **3**, 377 (1996).

[22] Q. H. Xiao, Ferro-Alloys **1**, 11 (1982).

[23] N. S. Zhang, Ferro-Alloys **6**, 1 (1986).

[24] C. C. Liu, Z. C. Jin, and C. J. Xu, J. Agricul. Machi. **25**, 28 (1994).

[25] H. Ma and J. B. Wang, Instrument Precision Theory, Beijing University of Aeronautics and Astronautics, Beijing (2014) pp. 364-365.

[26] J. Z. Zhang, Non-destructive Detecting Technology and Application, Science, Beijing (2010) pp. 130-150.

[27] Department of Mathematics of Tongji University. Higher Mathematics, Higher Education, Beijing (2007) pp. 113-123.